Impact of grain roughness on residual nonwetting phase cluster size distribution in packed columns of uniform spheres

Yukie Tanino,* Anelechi Ibekwe, and Dubravka Pokrajac
School of Engineering, University of Aberdeen, Aberdeen AB24 3UE, Scotland, United Kingdom

(Received 6 May 2020; accepted 29 June 2020; published 22 July 2020)

We imaged the pore-scale distribution of air and water within packed columns of glass spheres of different textures using x-ray microcomputed tomography after primary drainage and after secondary imbibition. Postimbibition residual air saturation increases with roughness size. Clusters larger than a critical size of about 15 to 40 pores are distributed according to a power law, with exponents ranging from $\tau = 2.29 \pm 0.04$ to 3.00 ± 0.13 and displaying a weak negative correlation with roughness size. The largest cluster constitutes 7 to 20% of the total residual gas saturation, with no clear correlation with roughness size. These results imply that activities that enhance grain roughness by, e.g., creating acidic conditions in the subsurface, will promote capillary trapping of nonwetting phases under capillary-dominated conditions. Enhanced trapping, in turn, may be desirable in some engineering applications such as geological CO_2 storage, but detrimental to others such as groundwater remediation and hydrocarbon recovery.

DOI: 10.1103/PhysRevE.102.013109

I. INTRODUCTION

Displacement of one fluid by another within a porous medium is relevant to many processes such as oil and gas recovery from hydrocarbon reservoirs, CO_2 storage in deep saline aquifers, gas transport in fuel cells, nonaqueous phase liquid contaminant transport in groundwater aquifers, and water infiltration into soils. Immiscible displacement encountered in these applications is influenced, at the pore scale, by the properties of the grains (size distribution, roughness, mineralogy) and how they are arranged (pore topology and geometry) [e.g., 1–5], the properties of the fluids (chemical and physical constituents, which in turn alter fluid-fluid-grain contact angle, fluid-fluid interfacial tension, viscosity, and density) [e.g., 6–8], the fractional volumes of the fluids initially occupying the pores [e.g., 6,9,10], and the velocity of the fluids [e.g., 11,12].

Of these, the dependence on grain roughness has received the least attention because micron- and nm-scale features are difficult to measure and even more difficult to vary systematically on numerous grains that constitute a porous sample of physically meaningful size. A limited number of studies have attributed differences in two-phase flow behavior between three-dimensional (3D) porous media to differences in grain roughness, but they are generally inconclusive because other parameters such as mineralogy, pore geometry, and grain size were varied simultaneously [e.g., 3,13]. Where experiments were performed on idealized porous media, e.g., packed beds of glass spheres, only two conditions—smooth vs acid-treated (rough) beads—were considered [14–16]. More recently, several studies have explored the impact of pore surface roughness on two-phase flow using purpose-built micromodels [17,18]. While these studies provide valuable insight into pore-scale displacement mechanisms, capillary trapping (snap-off) in two-dimensional (2D) systems differs from that in 3D systems [13,19], and the extent to which findings from 2D micromodels can be extrapolated to 3D media is not clear.

In this paper, we present laboratory measurements of the pore-scale distribution of air clusters established by secondary imbibition in packed columns of glass particles that were either in their original state (surface treatment R0) or mechanically pretreated to introduce nm-scale features (treatments R1, R3, and R4). We demonstrate that pore configuration remained constant across samples by comparing the porosity, the diameter and volume distributions of the pores and the grains, and the mean pore coordination number in each packed column (Sec. III A and Appendix A). The cluster size distribution in each sample is presented, and a power law fitted to clusters above a critical size (Sec. III B). Similarly, residual saturation is presented as a function of the characteristic roughness size and compared against percolation thresholds in idealized lattices (Sec. III C).

II. MATERIALS AND METHODS

Experiments were performed on $L = 38$-mm-long, 21-mm-diameter packed columns of soda-lime glass spheres (Mo-Sci Corporation, USA; 850- to 1000-μm diameter range). The test fluids and the sample holder are the same as those used in [20,21]. Following a protocol we developed previously [20], the surface of the spheres was mechanically altered by tumbling them in a barrel lined with sandpaper of mean grit diameter $d_s = 201$, 18.3, or 12.6 μm for a period of either $t_t = 4$ or 12 h; the specific combinations of grit size and tumbling duration considered in the present experiments are summarized in Table I. Further details of the particle

*ytanino@abdn.ac.uk

TABLE I. Basic properties for each roughness condition.

Surface treatment	d_s[a] (μm)	t_t[b] (h)	k [20] (μm^2)	ξ[c] (nm)
R0			460 ± 27	14.1 ± 2.7
R1	201	12	438 ± 19	26.9 ± 1.4
R3	18.3	12	399 ± 14	33.1 ± 1.9
R4	12.6	4	364 ± 10	34.3 ± 1.6

[a]Mean grit diameter of the sandpaper used to texture the particles.
[b]Tumbling duration.
[c]Mean integral length scale of scanning electron microscopy (SEM) images acquired previously [20]. The reported uncertainty is the standard error of the mean. The values reported here deviate slightly from those reported in [20] for two reasons: (a) a flat-field correction was not applied previously, which tends to artificially elevate r_0, and (b) a different radial-averaging algorithm was used.

texturing apparatus and method can be found in [20]. We also considered untreated spheres (surface treatment R0).

Following Ibekwe *et al.* [20], we use ξ, the median integral length scale of the grain surface captured in SEM images acquired previously [20] at image pixel size of 6.7 nm, as a proxy for the vertical size of the grain roughness. ξ was computed as follows.

(1) A flat field correction was applied to the images to eliminate image-scale gradients in illumination using MATLAB's imflatfield.m function using Gaussian smoothing with a standard deviation of 250 pix (1667 nm) to approximate the gradients.

(2) The two-point autocorrelation function, $Z(m, n)$, where (m, n) are the lags in the two orthogonal directions, was computed for each corrected image using the Wiener-Khintchine theorem [e.g., 22] and MATLAB's fft2.m and ifft2.m functions [23].

(3) $Z(m, n)$ was averaged at fixed radii, $r\,(=\sqrt{m^2+n^2})$, using Fisher [24]'s radialavg.m algorithm to calculate the one-dimensional isotropic autocorrelation function, $\hat{Z}(r)$.

(4) The integral length scale, ξ, was evaluated as

$$\xi = \int_0^{r_0} \hat{Z}\, dr, \tag{1}$$

where radial lag $r = r_0$ is the first zero crossing.

The median integral length scale calculated as described above increases from $\xi = 14.1 \pm 2.7$ for treatment R0 to 34.3 ± 1.6 nm for treatment R4 ($\pm$ standard error); values for the four treatments are presented in Table I.

A. Displacement sequence

The test fluids were air and tap water in all experiments. Previous *in situ* contact angle measurements using the same test fluids confirm that the water–air–glass bead system is water wetting [21].

For each experiment, a fresh pack was prepared by gradually pouring glass spheres treated according to one of the four treatments into a water-filled polycarbonate column while continuously tapping the column from the side until a 38-mm-long pack was assembled. The permeability of the resulting packs varies between treatments, decreasing with increasing

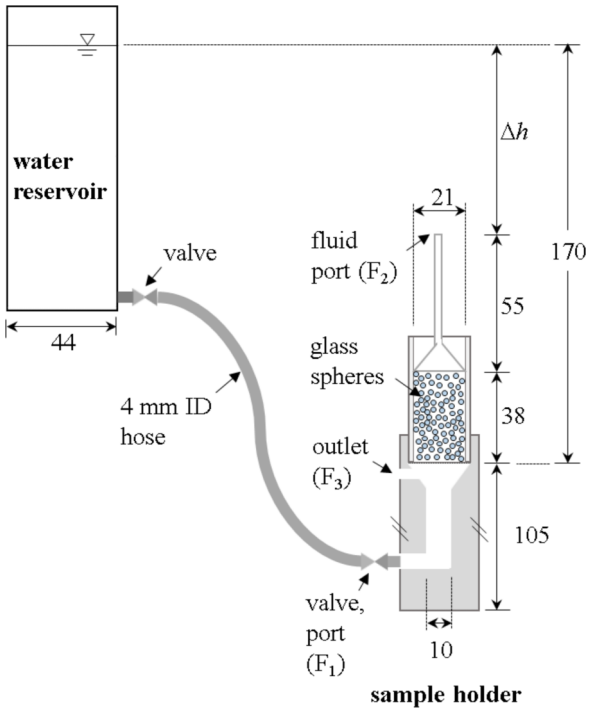

FIG. 1. Laboratory setup to establish initial and residual air saturation in the sample. Fluid port F_2 remained open to the atmosphere throughout each experiment. During drainage, the sample holder was disconnected from the water reservoir allowing water to drain freely from port F_1. During imbibition, the sample holder was connected to the water reservoir as depicted. All numbers indicate lengths in units of mm; all cross sections are circular. Not to scale.

ξ from $k = 460 \pm 27\,\mu$m^2 at $\xi = 14.1$ nm (R0) to $k = 364 \pm 10\,\mu$m^2 at $\xi = 34.3$ nm (R4) ([20], Table I). The pack was oriented vertically throughout each experiment.

Primary drainage was initiated by opening a valve below the packed column (fluid port F_1 in Fig. 1) to allow water to be drained from the bottom by gravity and air to enter from the top of the column (port F_2). After 24 to 428 h from the onset of drainage, the sample holder was carefully moved to a x-ray microcomputed tomography (μCT) scanner and scanned (see Sec. II B for details). The variation in the lag between the onset of drainage and the imaging was due to the availability of the μCT scanner; sensitivity tests over nine days confirmed that gas saturation remains static for at least that period [25].

After the scan, the sample holder was connected to a constant-head water reservoir via a flexible hose and positioned so that the lower face of the packed column was 170 mm below the free surface in the reservoir (Fig. 1). Secondary imbibition was initiated by opening the bottom valve (F_1) and allowing water to flow from the reservoir into the sample holder by gravity. Initially, outlet F_3 was open to purge the air in the flow line between the valve F_1 and the bottom of the pack. During this period, dispensed water flowed along the bottom face of the pack and out of the outlet; water invasion into the pack was by spontaneous imbibition. Subsequently, outlet F_3 was closed and all subsequent flow was directed into the sample (forced imbibition). Valve F_1 was closed after 100 to 125 mL of water was dispensed, and

the sample holder was disconnected from the flow lines. The sample holder was returned to the μCT scanner and scanned 24 to 341 h from the onset of imbibition.

Displacement experiments were performed on eight independent packs in total, two per surface treatment. All displacement experiments were conducted at ambient temperature and pressure. The Bond number remained approximately constant across all experiments at

$$\mathrm{Bo} = \frac{\rho_w g \langle d_b \rangle_n^2}{\sigma} \approx 0.013, \tag{2}$$

where g is gravitational acceleration, σ (=72 mN/m [26]) is the air-water interfacial tension, the density contrast between the phases was approximated by the density of water at 20°C, ρ_w (=998.2 kg/m^3 [27]), and the characteristic vertical length scale was taken to be the network-averaged pore body diameter ($\langle d_b \rangle_n$ = 294 to 315 μm, Table IV). The theoretical length of the largest residual cluster is given by [28]

$$\xi_B = \mathrm{Bo}^{-\nu/(1+\nu)} \langle d_b \rangle_n, \tag{3}$$

where $\nu = 0.88$ is the critical exponent for the correlation length in random 3D percolation processes ([29,30] and references therein). Substituting in Eq. (2), we obtain $\xi_B \approx 2360\,\mu$m for the present experiments, which is an order of magnitude smaller than the dimensions of the sample and the analyzed subvolume (Sec. II B), suggesting that the sample size did not suppress the size of the clusters.

The rate of the forced imbibition is characterized by the microscopic capillary number,

$$\mathrm{Ca} = \frac{\mu_w U_w}{\sigma}, \tag{4}$$

where μ_w (=1.0020 mPa s [31]) is the dynamic viscosity of water at 20 °C and U_w is the Darcy velocity of the imbibing water which, at steady state, is given by

$$U_w(\xi) = k_w(\xi, S_{gr}) \frac{\rho_w g}{\mu_w} \frac{\Delta h}{L}, \tag{5}$$

where Δh (=77 mm) is the drop in hydraulic head across the sample (Fig. 1) and $k_w(\xi, S_{gr})$ is the permeability of the sample to water at residual saturation. $k_w(\xi, S_{gr})$ is not known, but assuming that $k_w(\xi, S_{gr})/k(\xi) = O(1)$ and independent of roughness size yields velocities that decrease weakly with increasing ξ from $U_w \sim 9.0$ mm/s (R0) to 7.2 mm/s (R4); Ca proportionally decreases with increasing ξ from Ca $\sim 1.3 \times 10^{-4}$ to 1.0×10^{-4} (Table III).

B. Pore-scale image acquisition and segmentation

3D tomograms were acquired from the air-water-glass systems at a voxel size of 10 μm using a Zeiss XRadia Versa 410 3D μCT scanner with a 140-kV, 10-W x-ray source housed in the School of Engineering at University of Aberdeen. Each scan comprised 3200 projections. Using Avizo 9.0 software, the raw tomograms were first filtered with a $3 \times 3 \times 3$ kernel size median filter then segmented into air, water, and glass phases with the seeded watershed algorithm. For each scan, a cylindrical subvolume 1000 voxels in diameter and 1000 voxels in vertical length was analyzed (see Fig. 3).

The sizes of the grains, the pore bodies, and the pore constrictions (throats) that connect them were evaluated from each postimbibition scan as follows. The distribution of grain diameters in each pack was estimated using the grain partitioning algorithm implemented in Avizo 9.0. In brief, a $600 \times 600 \times 600$ voxel cubic region of interest (ROI) centered on the vertical axis of each tomogram was denoised using a $3 \times 3 \times 3$ kernel size median filter, then segmented into grains and fluid phases. The boundaries between the grains were identified using a combination of the Euclidean distance maps and watershed transforms. The porosity of the pack, ϕ, is taken to be the number fraction of voxels of the analyzed subvolume not occupied by grains. To exclude grains that partially fall outside the ROI from biasing the result, grain diameters are calculated only from grains the sphericity of which falls within the range $0.95 \leqslant \Psi < 1.05$.

To characterize the geometry and topology of the pore space, voxels occupied by fluid in a $640 \times 640 \times 901$ voxel cuboid were partitioned into pore bodies and pore throats using the maximum ball algorithm and network extraction algorithm developed by Dong and Blunt [32] and reimplemented by Raeini *et al.* [33]. Further details of the extracted networks and their analysis can be found in Appendix A.

TABLE II. Grain properties determined from postimbibition μCT images.[b]

Pack [a]	ϕ (%)	$\langle d_g \rangle_n$ (n) (μm)
R0 (1)	36.7	932 ± 3 (250)
R0 (2)	35.0	932 ± 2 (249)
R1 (1)	35.8	931 ± 2 (251)
R1 (2)	35.4	931 ± 2 (247)
R3 (1)	35.6	931 ± 2 (252)
R3 (2)	35.5	932 ± 2 (253)
R4 (1)	35.1	933 ± 2 (247)
R4 (2)	36.5	926 ± 2 (258)

[a](1) and (2) denote packs 1 and 2 for each treatment regime.
[b](ϕ, $\langle d_g \rangle_n$) are mean porosity and number-averaged grain diameter in the imaged region. Reported uncertainty in $\langle d_g \rangle_n$ is the standard error of the mean over n grains.

III. RESULTS AND DISCUSSION

A. Grain and pore size distribution

The porosity as computed from the μCT scans varies from ϕ = 35.0 to 36.7% (Table II), which is in excellent agreement with the porosity of random close packing of spheres ([34] and references therein). ϕ of our samples does not display a significant correlation with roughness size, contrary to previous observation that a randomly packed bed of ground nylon spheres has a higher ϕ—albeit by only 0.7% of the bulk volume for close packings—than a random bed of polished plexiglass spheres [35].

The distributions of grain diameters d_g (a); equivalent diameters of pore bodies, d_b, and pore throats, d_t (b); and pore body volumes, V_b (c) are presented in Fig. 2 for each treatment. Between 95 and 99% of grains in each pack have diameters within the range $850 < d_g < 1000\,\mu$m specified in the product specification [Fig. 2(a)], further validating the segmentation and grain partitioning algorithm. For convenience, the mean grain diameter in each scan, $\langle d_g \rangle_n$, is reported in

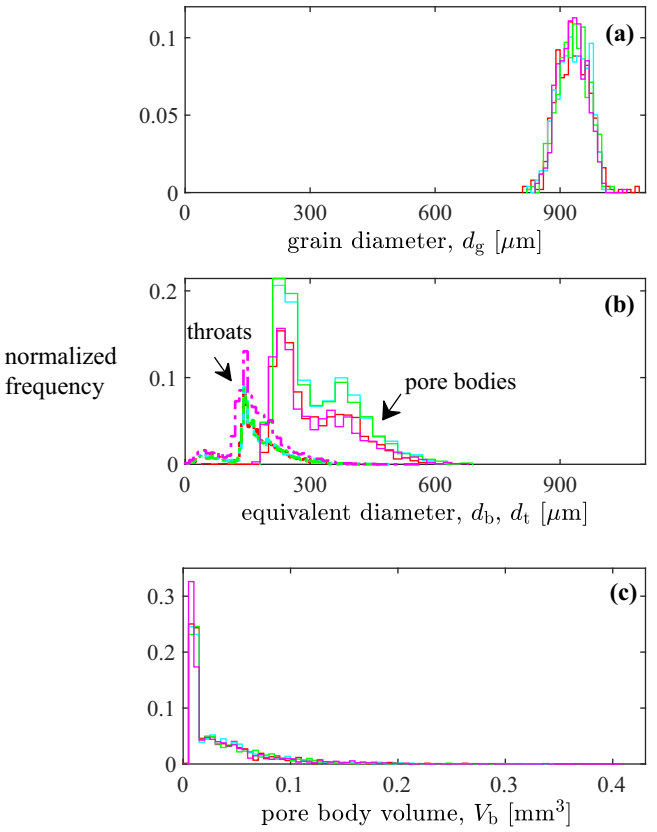

FIG. 2. Distributions of (a) the grain diameter, (b) the equivalent diameters of pore bodies (solid line) and pore throats (dash-dotted), and (c) pore body volumes for R0 (red), R1 (cyan), R3 (green), and R4 (magenta). Bin widths were selected according to the Freedman-Diaconis rule [36] as implemented in MATLAB.

Table II. In this paper $\langle\rangle_n$ denotes a number average over a μCT scan or a pore network extracted from it; $\langle\rangle_V$ denotes a volume-weighted average (Appendix A). The network-averaged pore body diameters ($\pm$ standard deviation) vary between $\langle d_b\rangle_n = 294 \pm 93$ [pack R4(2)] and $315 \pm 89\,\mu$m [R1(1)], in excellent agreement with a mean pore diameter of $\langle d_b\rangle_n = 326\,\mu$m in packed columns of uniform, $\langle d_g\rangle_n = 880\,\mu$m spheres reported elsewhere [13].

There is no observable difference in d_g, d_b, d_t, or V_b as a function of ξ, confirming that observed trends reported in Secs. III B and III C are due to differences in grain roughness rather than pore configuration.

B. Cluster size distribution

Figure 3 presents the pore-scale distribution of the air phase after primary drainage (top) and after imbibition (bottom) in one of the two packs for each treatment regime (i.e., R0, R1, R3, and R4); different ganglia sizes are depicted with different colors. As expected, much of the air saturation after drainage is in the form of a single, large, continuous volume of air that spans the entire imaging region (red). A few, small nonpercolating ganglia are depicted by other colors.

In contrast, air saturation after imbibition is in the form of many, discrete clusters of different sizes uniformly distributed across the length of the packed column (e.g., Fig. 3, bottom row). No cluster spans the entire length of the field of view, indicative of a residual (i.e., nonpercolating) state consistent with the uniformly water-wetting state of our air-water-glass system.

Because the cylindrical subvolume did not span the entire cross section of the packed column, many of the captured clusters are truncated, resulting in cluster distributions that,

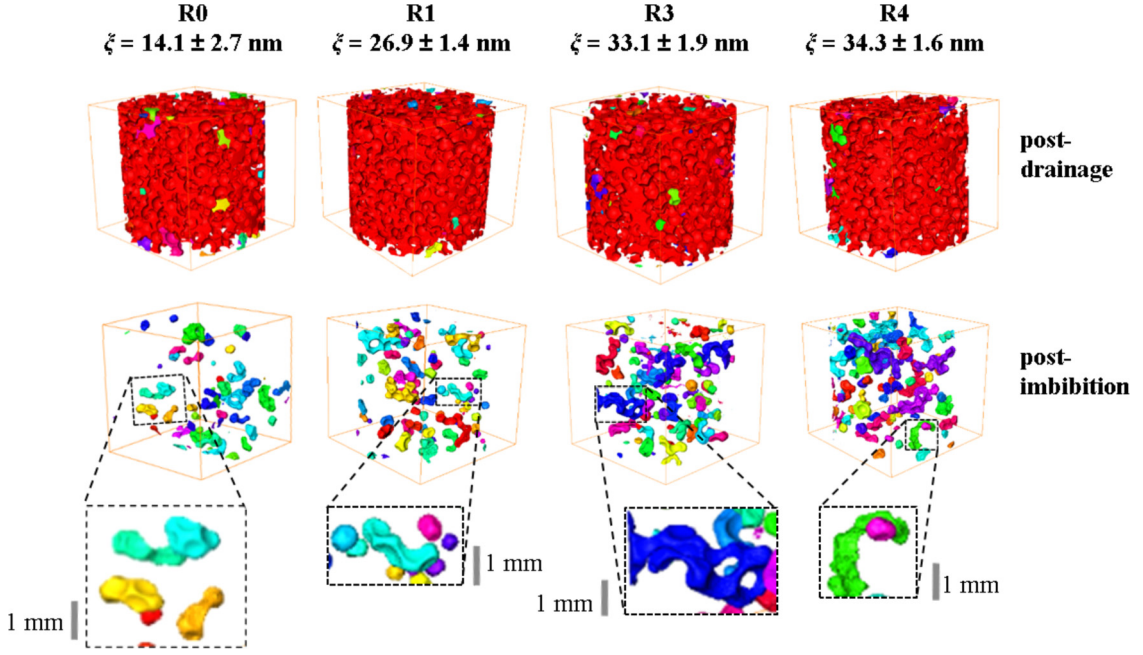

FIG. 3. 3D renderings of post-drainage (top row) and postimbibition (bottom) air clusters for packs R0(2), R1(1, postdrainage; 2, postimbibition), R3(1), and R4(1). Different colors depict different cluster sizes; the orange bounding boxes correspond to 10 × 10 × 10 mm. Water and grains are not shown. Insets show magnified images of selected air clusters.

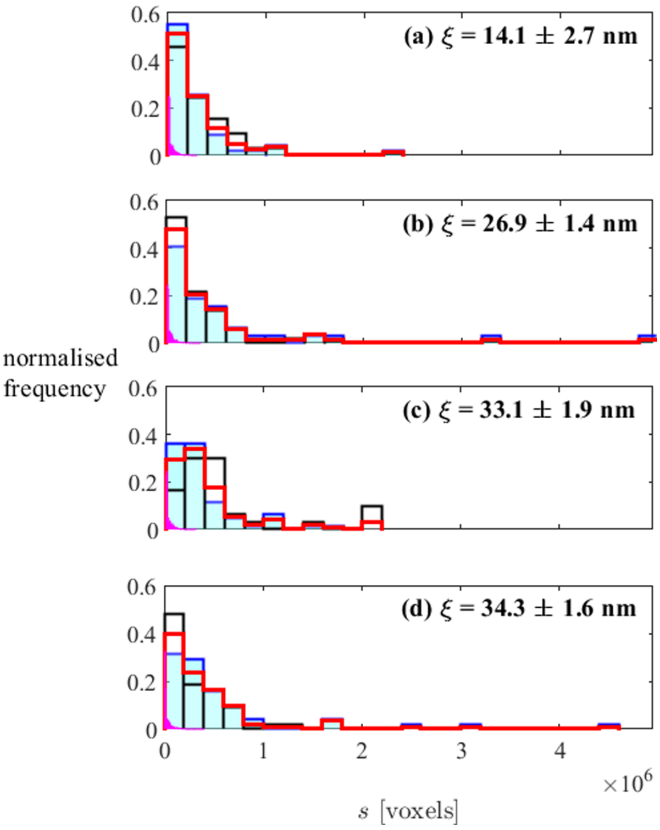

FIG. 4. Postimbibition cluster size distribution for R0 (a), R1 (b), R3 (c), and R4 (d). Packs 1 and 2 are depicted by filled (blue) and open (black) bars, respectively; red bars depict the combined distribution of clusters in both packs. The ordinate is the number of clusters in the bin divided by the total number of clusters in each data set; the bin size is 2×10^5 voxels for all histograms. Recall that 1 voxel $= (10\,\mu\text{m})^3$. Superposed are distributions of pore body volumes from Fig. 2(c) (magenta).

at first glance, appear to be dominated by small clusters of size $1 \leqslant s \leqslant O(100)$ voxels. To avoid truncated clusters from erroneously skewing the distribution, clusters that fall within the equivalent cluster radius [$d_c/2$, Eq. (B1)] or the mean grain radius ($\langle d_g \rangle_n/2$) of the circumference of the imaged subvolume or within $\langle d_g \rangle_n$ of the top and bottom boundary of the subvolume are excluded from consideration in the analysis that follows in this section (Sec. III B). In addition, clusters smaller than the smallest V_b in the corresponding pore network are excluded from consideration because capillary trapping cannot yield clusters smaller than the size of a single pore. The relative number of clusters excluded according to these criteria are summarized in Table V.

Figure 4 presents the normalized frequency of gas clusters of particular volume at residual saturation, $n(s)/N$, where $n(s)$ is the number of air clusters of volume s and N is the total number of (untruncated) clusters. Superposed in Fig. 4 are distributions of V_b (magenta); these are identical to those presented in Fig. 2(c).

It is readily apparent that the clusters are significantly larger than a single pore body. Indeed, the pore body volume distribution can barely be discerned because the largest ganglia is one order of magnitude larger at $\max\{s\} = O(1 \text{ to } 5) \times 10^6$ voxels (Table III) than the largest $V_b = O(2 \text{ to } 4) \times 10^5$ voxels across all packs. Similarly, the largest ganglia is a factor of 65 [pack R0(2)] to 320 [R1(1)] larger than the median V_b. The volume of the largest ganglia broadly increases with ξ, but the correlation is not statistically significant.

In units of fractional volume of the total residual gas volume, the largest cluster constitutes $\max\{s\} = 7\%$ [R3(1)] to 20% [R1(1)]. These values are comparable to those measured by Andrew *et al.* [5] in water–supercritical CO_2–rock systems, where 6 to 26% of residual saturation was found to be associated with the largest ganglion in two sandstones and three limestones.

Power-law regime

Invasion percolation theory [28,37,38] predicts that residual cluster sizes are distributed according to a power law of the form

$$n(s) \sim s^{-\tau}. \tag{6}$$

TABLE III. Postimbibition cluster properties. Power laws were fitted to the combined set of clusters from packs 1 and 2 at each treatment condition. R is the Pearson correlation coefficient of ($\lg_{10} s$, $\lg_{10} P_s$) for $s \geqslant 5 \times 10^5$ voxels.

					max{s}		Power-law regime		
Pack	Ca ($\times 10^{-4}$)	N[a]	S_{gi} (%)	S_{gr} (%)	(voxels)	(%)[b]	τ	N^*[c]	R
R0 (1)	1.3	47	66.6	5.75	2215585	13.0	3.00 ± 0.13	16	−0.9736
R0 (2)		33	68.0	4.38	1008962	8.2			
R1 (1)	1.2	32	65.7	8.68	4959629	19.8	2.29 ± 0.04	21	−0.9899
R1 (2)		51	78.8	6.22	1487821	8.4			
R3 (1)	1.1	61	63.5	8.78	1672660	6.6	2.61 ± 0.09	25	−0.9648
R3 (2)		30	61.2	7.70	2198646	10.0			
R4 (1)	1.0	51	68.0	11.44	4456624	13.8	2.43 ± 0.03	29	−0.9928
R4 (2)		54	63.5	7.98	1790368	7.6			

[a]The total number of clusters considered in Figs. 4 and 5 and the calculation of τ. Details of clusters excluded from consideration can be found in Appendix B.
[b]Percentage of total residual gas volume.
[c]The number of clusters of size $s \geqslant 5 \times 10^5$ voxels.

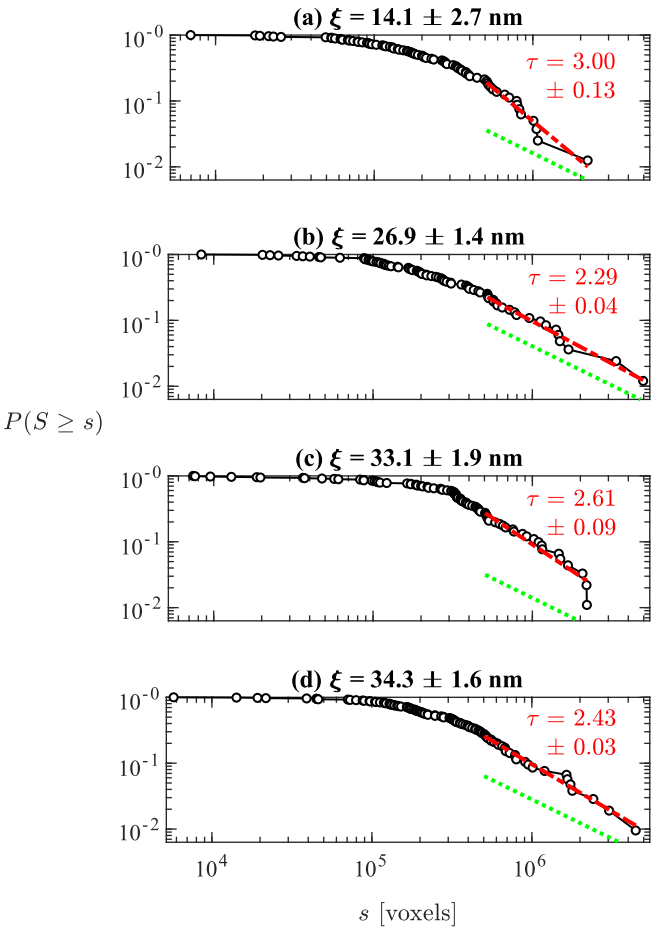

FIG. 5. Complementary cumulative distribution function of the cluster size for R0 (a), R1 (b), R3 (c), and R4 (d). Superposed are power laws of the form Eq. (8) with $\tau = 2.189$ determined for 3D cubic lattices [42] (green dotted) and best-fit τ to data larger than or equal to $s \geqslant 5 \times 10^5$ voxels (red dash-dotted). Recall that 1 voxel $= (10\,\mu\text{m})^3$.

More recently, a number of laboratory studies have reported a power-law distribution at intermediate values of s [e.g., 5,39–41].

A power-law regime is not readily apparent from Fig. 4 because the field of view did not span the entire cross section of the packed column and only 80 to 105 nontruncated clusters could be captured for each ξ between the two packs (Table III). We thus considered the complementary cumulative distribution function of the cluster size, $P(s) = \Pr(S \geqslant s)$, instead:

$$P(s) = \frac{\sum_s^\infty n(s')}{\sum_1^\infty n(s')}. \tag{7}$$

$\int_s^\infty s'^{-\tau} ds' = -s^{1-\tau}/(1-\tau)$ if $1 - \tau < 0$ and, accordingly, it follows from Eqs. (6) and (7) that

$$P(s) \sim s^{1-\tau} \tag{8}$$

within the power-law regime.

Figure 5 presents $P(s)$ for each ξ considered. At all ξ, $P(s)$ displays a power-law dependence on s above a critical threshold of around $s \approx (3 \text{ to } 5) \times 10^5$ voxels, which corresponds to 0.3 to 0.5 mm^3 and 15 to 40 pores (based on median pore body volume, Table IV). Estimates of lower cutoff of the power-law regime reported in the literature vary by orders of magnitude, from, e.g., 10^{-7} mm^3 for n-decane/brine in Bentheimer sandstone [40] to 0.03 mm^3 identified by Andrew *et al.* [5] for supercritical CO_2/brine in five sandstones and limestones, of which one is Bentheimer sandstone. Notwithstanding, Andrew *et al.*'s cutoffs correspond to 57 to 430 pores (based on modal pore body volume), which we interpret to be comparable to the present results.

A single, conservative cutoff of $s = 5 \times 10^5$ voxels (0.5 mm^3) was used to fit a straight line to $(\lg_{10} s,\ \lg_{10} P(s))$ data for each ξ in the least-squares sense (red, dash-dotted lines, Fig. 5). The correlation is highly significant for all ξ (Pearson correlation coefficient $|R| > 0.96$, Table III). The best-fit τ was evaluated from the gradient of the line; the uncertainty in τ is taken to be the uncertainty in the gradient [43].

The best-fit values of τ range from $\tau = 2.29 \pm 0.04$ to 3.00 ± 0.13, and display a weak, negative correlation with ξ. These values are equal to or larger than values between $\tau = 2.11$ and 2.28 reported by Mohammadian [41] for air-water in packed columns of glass spheres. Values reported in the literature in other types of 3D media are similarly smaller than the present values, e.g., $\tau = 2.189$ for cubic lattices [42] (dotted line, Fig. 5), $\tau = 2.05$ for n-octane/brine in both Doddington and Clashach sandstones [44], and $\tau = 1.1$ for n-decane/brine in Bentheimer sandstone [40]. Andrew *et al.* [5] found exponents ranging from $\tau = 1.83$ to 2.29 for supercritical CO_2/brine in a set of three limestones and Bentheimer and Doddington sandstones, with τ decreasing monotonically with increasing pore coordination number from $\langle z \rangle_V = 5.17$ to 20.71.

However, as discussed above, the aforementioned studies fit the power-law regimes to widely different ranges of cluster sizes. Estimates of τ are sensitive to both the range of s included in the fitting and the objective function used in the optimization [45]. In particular, Mohammadian [41] demonstrates that τ estimated by fitting a power law to the cumulative distribution of volume-weighted cluster sizes, $s\,n(s)$, decreases monotonically as the largest cluster size considered in the power law is reduced. Further insight requires additional cluster size distribution data over a larger field of view and in larger samples. This is a topic for future work, involving more sophisticated imaging approaches.

C. Residual saturation

Initial gas saturations, S_{gi}, were computed by counting the number of voxels occupied by air and dividing it by the number of nonsolid voxels. The residual gas saturation for each scan, S_{gr}, was computed by summing the number of voxels occupied by each air cluster (both truncated and untruncated clusters) and dividing it by ϕ, as estimated below, and the number of voxels in the 1000 × 1000-voxel cylindrical subvolume.

Values of (S_{gi}, S_{gr}) for each scan are summarized in Table III. $S_{gr} \approx 5.1\%$ in the smooth (untreated) samples (R0) are in excellent agreement with residual air saturations of $S_{gr} = 4$ to 6% measured in packed beds of uniform glass spheres of comparable diameter by Geistlinger *et al.* [13] at

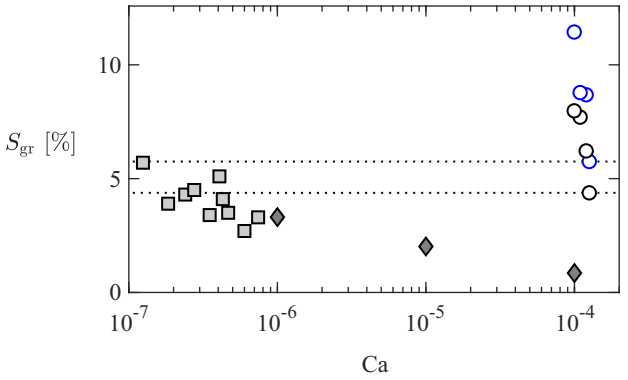

FIG. 6. Residual gas saturation as a function of Ca in packed beds of uniform glass spheres measured in the present study (circles), by Geistlinger *et al.* [13] (squares; air–water, 880-μm glass particles), and by Suekane *et al.* [46] (diamonds; N_2/water, 600-μm spheres). Color indicates pack in the present data: pack 1 (blue) and 2 (black). Dotted lines indicate S_{gr} in the two untreated samples (R0).

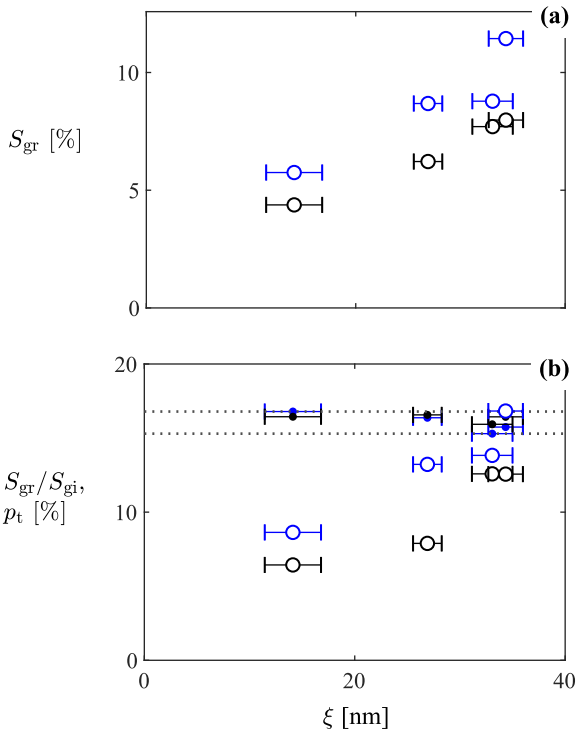

FIG. 7. Residual gas saturation (circles) as a percentage of the pore volume (a) and initial gas saturation (b) as a function of roughness size. Superposed are predicted percolation thresholds [dots; Eq. (9)]; dotted lines demarcate the minimum and maximum values predicted. Color indicates pack: pack 1 (blue) and 2 (black).

low Ca ($\leqslant 4.0 \times 10^{-7}$) (Fig. 6, squares). Previous secondary imbibition experiments in packed beds of glass spheres have shown that where residual gas saturation is established by forced imbibition at low Ca ($=10^{-6}$) the gas clusters remain immobile against subsequent flow of water up to rates as high as Ca $= 10^{-4}$ [46]; similar behavior has been documented in water-oil-sandstones [e.g., 47]. Figure 6 suggests that, in the present experiments, gas clusters were established by spontaneous imbibition prior to the invasion of the bulk water front at Ca $= O(10^{-4})$ (see Sec. II A). Further insight requires additional experiments over a wide range of imbibition rates ($10^{-8} \leqslant$ Ca $\leqslant 10^{-2}$).

Residual saturation increases with roughness size under conditions considered presently, roughly doubling in volume from $S_{gr} = 5.1\%$ (R0) to 9.7% (R4) as ξ increased from $\xi = 14.1$ to 34.3 nm [Fig. 7(a)]. While it is widely speculated in the literature that grain roughness promotes snap-off and hence elevates S_{gr} under strongly water-wetting conditions, here we provide experimental evidence of the effect that can be attributed unambiguously to changes in grain roughness alone.

Capillary trapping is often modeled as a percolation process. Figure 7(b) compares measured residual gas saturation (normalized by its initial saturation) against bond percolation

TABLE IV. Basic properties of the pore networks extracted from the μCT scans.[a]

Pack	$\phi_{network}$ (%)	$k_{network}$[b] (μm^2)	Mean coordination number[c] $\langle z\rangle_n$	$\langle z\rangle_V$	n_b	Pore body volume V_b Min. (voxels)	Max. (voxels)	Median (voxels)	$\langle d_b\rangle_n$[d] (μm)	p_t[e]
R0 (1)	35.5	423.0	6.80 ± 2.5	8.93 ± 2.9	699	6680	290241	15455	306 ± 88	0.168
R0 (2)	36.7	482.0	6.95 ± 2.6	9.12 ± 3.0	729	108	229764	16222	309 ± 86	0.164
R1 (1)	36.2	496.3	6.98 ± 2.6	9.16 ± 3.0	731	6784	341360	19005.5	315 ± 89	0.164
R1 (2)	36.2	465.8	6.95 ± 2.6	9.06 ± 2.8	705	6517	216346	17384	314 ± 91	0.166
R3 (1)	36.3	458.0	7.11 ± 2.8	9.81 ± 3.3	670	6068	311516	18253	314 ± 97	0.153
R3 (2)	36.9	495.4	7.13 ± 2.7	9.42 ± 3.1	697	6647	254496	17422	312 ± 87	0.159
R4 (1)	37.5	521.4	7.02 ± 2.8	9.53 ± 3.3	673	6217	407513	17472	315 ± 95	0.157
R4 (2)	32.9	321.0	6.53 ± 2.7	9.13 ± 3.2	733	5387	366625	13139	294 ± 93	0.164

[a] $\langle\ \rangle_n$ denotes number average.
[b] The permeability of the network, $k_{network}$, was predicted by the two-phase flow pore-network simulator developed in [54].
[c] The reported uncertainty in the mean coordination numbers is $\pm$ standard deviation over n_b pore bodies in the network.
[d] The reported uncertainty is $\pm$ standard deviation.
[e] Predicted by Eq. (9).

thresholds for uniform, regular, 3D lattices [48]:

$$p_t \approx \frac{1.5}{\langle z \rangle_V}; \tag{9}$$

following Tanino and Blunt [2] we use the volume-weighted mean coordination number, $\langle z \rangle_V$, evaluated from pore networks extracted from the μCT scans here. Details of $\langle z \rangle_V$ can be found in Appendix A. $\langle z \rangle_V$ does not display a monotonic dependence on ξ (Table IV) and, accordingly, the percolation threshold is approximately constant at $p_t \approx 16.2 \pm 0.5$ ($\pm$ standard deviation) across the eight packs considered [dotted lines, Fig. 7(b)].

p_t accurately predicts measured S_{gr}/S_{gi} within experimental uncertainty at the largest $\xi = 34.3$ nm, but overestimates residual saturation at smaller ξ, with the discrepancy increasing as ξ decreases (i.e., as the grains become smoother). Note that if we use the number-averaged coordination number, $\langle z \rangle_n$, instead of $\langle z \rangle_V$ in Eq. (9), both the predicted p_t and the discrepancy will be even greater. In contrast, p_t was shown to underestimate residual saturation in limestones and sandstones within the range $0.39 \leqslant S_{nwr}/S_{nwi} \leqslant 0.59$ [2]. Grain roughness in real rock—particularly in microporous limestones such as those considered in [2]—is expected to be larger than the roughness of glass particles in the present experiments. It may be that Eq. (9) overestimates residual saturation at small ξ but underestimates residual saturation at large ξ. Further insight requires additional experiments using glass particles with larger ξ.

IV. CONCLUSIONS

We imaged the distribution of residual gas clusters after secondary imbibition in packed columns of systematically textured uniform spheres using μCT. Four surface textures were considered. The main findings are as follows.

(1) Residual gas clusters follow a power-law distribution for clusters larger than 15 to 40 pores.

(2) The best-fit power-law exponent broadly decreases with increasing roughness size from $\tau = 3.00 \pm 0.13$ to 2.43 ± 0.03.

(3) The largest cluster constitutes, on average, 11% of the total gas volume remaining after imbibition.

(4) Residual gas saturation increases with roughness size, even when the imbibition is initiated from initial water saturations of 20 to 40%.

The physics behind the correlation between cluster size distribution and roughness size remains an open question. Several studies have reported reduced residual nonwetting phase saturation in packed beds of smooth spheres compared to rough spheres [e.g., 15]. A popular explanation for this phenomenon is that roughness serves as pathways for precursor wetting layer flows [e.g., 18,49,50] and that, in their absence, capillary trapping by snap-off is reduced. However, wetting layers are already established at the onset of imbibition in the present experiments. An alternative explanation is that larger roughnesses are more likely to protrude from wetting layers, acting as capillary "pinning points" for wetting phase–nonwetting phase–solid contact lines [51]. It seems plausible that contact line pinning resists the displacement of the nonwetting phase and, at least under certain conditions, enhances capillary trapping [17]. Independently, roughness may also enhance capillary trapping by affecting wettability. For example, it may be that larger roughness gives rise to *smaller* advancing contact angles, which in turn favor snap-off. There is empirical evidence of such dependence: under strongly water-wetting conditions (equilibrium contact angles on a flat surface $<50^\circ$), effective advancing contact angles in polytetrafluoroethylene tubes were found to be smaller in tubes the walls of which were intensely roughened compared to those with slightly roughened walls [52]. Further insight requires dynamic imaging of imbibing water fronts at the $O(1)\,\mu$m scale, in 3D media, from a range of initial water saturations, imbibition rates, and surface textures.

We now return to one of the applications that motivates this study, geological CO_2 storage. Grain roughness in a geological reservoir—whether it be depleted oil reservoirs or deep saline aquifers—is expected to vary at all spatial scales ranging from the pore scale to the reservoir scale because mineralogical variations occur across these scales. Injection of fluids into a geological reservoir can create acidic solutions in the reservoir, which are known to enhance the roughness of different materials exposed to them. The present findings suggest that the interaction of grains with CO_2-saturated brine, which is carbonic acid, may promote the trapping of CO_2 by altering the surface texture of grains within a geological storage site.

All data used in this paper are available from the corresponding author on reasonable request.

ACKNOWLEDGMENTS

This material contains work supported by an Aberdeen Formation Evaluation Society student bursary and a Society of Petrophysicists and Well Log Analysts Foundation grant. A.I. was supported by the University of Aberdeen School of Engineering Elphinstone Ph.D. studentship. Pore-scale imaging was performed in the Oil & Gas Academy of Scotland x-ray microcomputed tomography facility at University of Aberdeen. The authors thank the two anonymous reviewers for their comments.

APPENDIX A: BASIC PROPERTIES OF THE PORE NETWORKS

The basic properties of the pore networks extracted from the μCT scans are summarized in Table IV. The porosity, $\phi_{network}$, and permeability, $k_{network}$, for the pore network extracted from scan R4(2) deviate from their average over the remaining seven networks by six and five standard deviations, respectively (Table IV). $\phi_{network}$ and $k_{network}$ of network R4(2) are significantly smaller than direct measurements of (ϕ, k) also. The remaining seven networks, however, display good agreement with laboratory measurement.

The topology of a pore network is described by the pore coordination number, z, which is the number of throats connected to a given pore body. Following Tanino and Blunt [2], the mean pore coordination number for each pore network was computed using two different probability mass functions, $p_Z(z)$, as $\langle z \rangle = \sum_{z=1}^{z_c} z\, p_Z(z)$. The smallest z for which the normalized frequency is less than 0.5% of the total number

TABLE V. Breakdown of clusters identified in postimbibition μCT scans.

	Number of clusters			
	All sizes		Smaller than min$\{V_b\}$	
Pack	Entire domain[a]	Excluded region[b]	Entire domain	Excluded region[b]
R0 (1)	10448	10399	10375	10373
R0 (2)	10164	10131	10081	10081
R1 (1)	14939	7617	14862	7572
R1 (2)	9944	9891	9868	9866
R3 (1)	7665	7576	7573	7545
R3 (2)	10126	10094	10079	10077
R4 (1)	6129	5996	6043	5961
R4 (2)	8518	8316	8433	8285

[a]The total number of clusters in the 1000 × 1000-voxel cylindrical subvolume.
[b]The total number of clusters within $\langle d_g\rangle_n$ of the top or bottom or within max$\{d_c, \langle d_g\rangle_n\}/2$ of the side of the cylindrical subvolume, where d_c is the equivalent diameter of each cluster [Eq. (B1)].

of pore bodies was chosen as the threshold, z_c, to prevent anomalously large z and isolated pore bodies from altering the estimate of the $\langle z\rangle$ dramatically [2]. A number-averaged pore coordination number, $\langle z\rangle_n$, was calculated using

$$p_Z(z) = \frac{n(z)}{\sum_{z=1}^{z_c} n(z)}, \tag{A1}$$

where $n(z)$ is the number of pore bodies with coordination number z. A volume-weighted mean coordination number, $\langle z\rangle_V$, was calculated using

$$p_Z(z) = \frac{\sum_{j\in S(z)} V_{b,j}}{\sum_{z=1}^{z_c}\sum_{j\in S(z)} V_{b,j}}, \tag{A2}$$

where $S(z)$ is the set of pore bodies with coordination number z, and $V_{b,j}$ is the volume of the jth pore body.

To prevent boundary effects from biasing the statistics, pore bodies within 470 μm ($\approx\langle d_g\rangle_n/2$, Table II) of the six sides of the cuboidal ROI were excluded in calculating $\langle z\rangle_n$ and $\langle z\rangle_V$ and the minimum, maximum, and median pore body volume (Table IV), nor are they included in the pore body diameter and volume distributions presented in Fig. 2. Pore throats that connect on both ends to pore bodies within 470 μm of an edge were similarly excluded from the distribution of their diameters [Fig. 2(b)].

In all eight networks, the modal coordination number is 5 and $\langle z\rangle_n = 7 \pm 3$ (standard deviation) (Table IV). This value is close to $\langle z\rangle_n = 6.6$ in a packed bed of uniform spheres of $\phi = 0.321$ prepared by removing 10% of spheres from a hexagonal closest pack [53]. The volume-weighted coordination number is consistently larger than $\langle z\rangle_n$, with a value of $\langle z\rangle_V =$ (9 to 10) $\pm$ 3 in all packs. The discrepancy between $\langle z\rangle_n$ and $\langle z\rangle_V$ reflects a strong positive correlation between pore volume and coordination number (i.e., larger pores have more throats connected to them).

APPENDIX B: SPATIAL DISTRIBUTION OF RESIDUAL GAS CLUSTERS WITHIN IMAGED SUBVOLUME

Table V summarizes the number of clusters in the entire 1000 × 1000-voxel cylindrical subvolume that was imaged and in the region near its edges that is excluded from consideration in Figs. 4 and 5 and the calculation of τ. In all packs but R1(1), 97.6–99.7% of clusters occurred in the excluded region, i.e., were centered within max$\{d_c, \langle d_g\rangle_n\}/2$ of the side of the cylindrical subvolume, where

$$d_c(s) = 2\left(\frac{s}{4\pi/3}\right)^{1/3} \tag{B1}$$

is the equivalent diameter of a cluster of size s, or within $\langle d_g\rangle_n$ of the top or bottom of the subvolume. In R1(1), the clusters in the excluded region constitute only 51% of the total number of clusters because the latter is elevated by a large number of small ($s < \min\{V_b\}$) clusters in an annular region around the side (not shown).

Similarly, 99 $\pm$ 0.3% of clusters are smaller than the smallest equivalent pore body diameter in the pore network extracted from that scan, although by volume they constitute only 0.4 to 2.2% of the total residual gas volume. Moreover, the majority of these small clusters fall within the excluded region (Table V, fifth column), consistent with our interpretation that many are larger clusters that appear small because they have been truncated by the imaging boundary.

[1] I. Chatzis, N. R. Morrow, and H. T. Lim, Magnitude and detailed structure of residual oil saturation, Soc. Petrol. Eng. J. **23**, 311 (1983).
[2] Y. Tanino and M. J. Blunt, Capillary trapping in sandstones and carbonates: Dependence on pore structure, Water Resour. Res. **48**, W08525 (2012).
[3] S. A. Bowden, Y. Tanino, B. Akamairo, and M. Christensen, Recreating mineralogical petrographic heterogeneity within microfluidic chips: Assembly, examples, and applications, Lab Chip **16**, 4677 (2016).
[4] N. C. Wardlaw, The effects of geometry, wettability, viscosity and interfacial tension on trapping in single pore-throat pairs., J. Canadian Petrol. Technol. **21**, 21 (1982).
[5] M. Andrew, B. Bijeljic, and M. J. Blunt, Pore-scale imaging of trapped supercritical carbon dioxide in sandstones and carbonates, Inter. J. Green. Gas Con. **22**, 1 (2014).

[6] Y. Tanino and M. J. Blunt, Laboratory investigation of capillary trapping under mixed-wet conditions, Water Resour. Res. **49**, 4311 (2013).

[7] M. Christensen and Y. Tanino, Enhanced permeability due to apparent oil/brine slippage in limestone and its dependence on wettability, Geophys. Res. Lett. **44**, 6116 (2017).

[8] Y. Tanino and M. Christensen, Imbibition capillary pressure and relative permeability of mixed-wet microporous rock: New insights from history matching, Transport Porous Media **129**, 121 (2019).

[9] C. H. Pentland, R. El-Maghraby, S. Iglauer, and M. J. Blunt, Measurements of the capillary trapping of super-critical carbon dioxide in Berea sandstone, Geophys. Res. Lett. **38**, L06401 (2011).

[10] N. Alyafei and M. J. Blunt, The effect of wettability on capillary trapping in carbonates, Adv. Water Resour. **90**, 36 (2016).

[11] Y. Tanino, X. Zacarias-Hernandez, and M. Christensen, Oil/water displacement in microfluidic packed beds under weakly water-wetting conditions: Competition between precursor film flow and piston-like displacement, Expts. Fluids **59**, 35 (2018).

[12] M. Christensen, X. Zacarias-Hernandez, and Y. Tanino, Impact of injection rate on transient oil recovery under mixed-wet conditions: A microfluidic study, E3S Web Conf. **89**, 04002 (2019).

[13] H. Geistlinger, I. Ataei-Dadavi, S. Mohammadian, and H.-J. Vogel, The impact of pore structure and surface roughness on capillary trapping for 2-D and 3-D porous media: Comparison with percolation theory, Water Resour. Res. **51**, 9094 (2015).

[14] B. Liang, I. M. Zarikos, W. B. Bartels, S. M. Hassanizadeh, and A. Clarens, Effect of nanoscale surface textures on multiphase flow dynamics in capillaries, Langmuir **35**, 7322 (2019).

[15] F. A. L. Dullien, C. Zarcone, I. F. Macdonald, A. Collins, and R. D. E. Bochard, The effects of surface roughness on the capillary pressure curves and the heights of capillary rise in glass bead packs, J. Colloid Interf. Sci. **127**, 362 (1989).

[16] K. Shellenberger and B. E. Logan, Effect of molecular scale roughness of glass beads on colloidal and bacterial deposition, Environ. Sci. Technol. **36**, 184 (2002).

[17] A. Mehmani, S. Kelly, C. Torres-Verdín, and M. Balhoff, Capillary trapping following imbibition in porous media: Microfluidic quantification of the impact of pore-scale surface roughness, Water Resour. Res. **55**, 9905 (2019).

[18] H. Geistlinger, I. Ataei-Dadavi, and H.-J. Vogel, Impact of surface roughness on capillary trapping using 2D-micromodel visualization experiments, Transport Porous Med. **112**, 207 (2016).

[19] K. Xu, T. Liang, P. Zhu, P. Qi, J. Lu, C. Huh, and M. Balhoff, A 2.5-D glass micromodel for investigation of multi-phase flow in porous media, Lab Chip **17**, 640 (2017).

[20] A. Ibekwe, Y. Tanino, and D. Pokrajac, A low-cost, non-hazardous protocol for surface texturing of glass particles, Tribol. Lett. **67**, 115 (2019).

[21] A. Ibekwe, D. Pokrajac, and Y. Tanino, Automated extraction of *in situ* contact angles from micro-computed tomography images of porous media, Comp. Geosci. **137**, 104425 (2020).

[22] C. Robertson and S. C. M. D. George, Theory and practical recommendations for autocorrelation-based image correlation spectroscopy, J. Biomed. Opt. **17**, 080801 (2012).

[23] T. Ursell, autocorr2d, MATLAB Central File Exchange (2018), retrieved June 12, 2019.

[24] D. J. Fisher, radialavg, MATLAB Central File Exchange (2016), retrieved June 20, 2019.

[25] A. Ibekwe, Impact of grain roughness on the pore scale distribution of immiscible fluids in porous media, Ph.D. thesis, University of Aberdeen, 2020.

[26] N. R. Pallas and Y. Harrison, An automated drop shape apparatus and the surface tension of pure water, Colloid. Surface. **43**, 169 (1990).

[27] F. E. Jones and G. L. Harris, Density of water formulation for volumetric standards calibration, J. Res. Natl. Inst. Stand. Technol. **97**, 335 (1992).

[28] D. Wilkinson, Percolation effects in immiscible displacement, Phys. Rev. A **34**, 1380 (1986).

[29] D. Wilkinson, Percolation model of immiscible displacement in the presence of buoyancy forces, Phys. Rev. A **30**, 520 (1984).

[30] D. S. Gaunt and M. F. Sykes, Series study of random percolation in three dimensions, J. Phys. A: Math. Gen. **16**, 783 (1983).

[31] L. Korson, W. Drost-Hansen, and F. J. Millero, Viscosity of water at various temperatures, J. Phys. Chem. **73**, 34 (1969).

[32] H. Dong and M. J. Blunt, Pore-network extraction from micro-computerized-tomography images, Phys. Rev. E **80**, 036307 (2009).

[33] A. Q. Raeini, B. Bijeljic, and M. J. Blunt, Generalized network modeling: Network extraction as a coarse-scale discretization of the void space of porous media, Phys. Rev. E **96**, 013312 (2017), https://github.com/aliraeini/pnextract.

[34] J. G. Berryman, Random close packing of hard spheres and disks, Phys. Rev. A **27**, 1053 (1983).

[35] G. D. Scott and D. M. Kilgour, The density of random close packing of spheres, J. Phys. D: Appl. Phys. **2**, 863 (1969).

[36] D. Freedman and P. Diaconis, On the histogram as a density estimator: L_2 theory, Z. Wahrscheinlichkeitstheorie verw Gebiete **57**, 453 (1981).

[37] D. Wilkinson and J. F. Willemsen, Invasion percolation: a new form of percolation theory, J. Phys. A: Math. Gen. **16**, 3365 (1983).

[38] M. M. Dias and D. Wilkinson, Percolation with trapping, J. Phys. A: Math. Gen. **19**, 3131 (1986).

[39] A. Georgiadis, S. Berg, A. Makurat, G. Maitland, and H. Ott, Pore-scale micro-computed-tomography imaging: Nonwetting-phase cluster-size distribution during drainage and imbibition, Phys. Rev. E **88**, 033002 (2013).

[40] S. Iglauer and W. Wulling, The scaling exponent of residual nonwetting phase cluster size distributions in porous media, Geophys. Res. Lett. **43**, 11253 (2016).

[41] S. Mohammadian, A micro-CT study of capillary trapping and pore-scale quantification of effective mass transfer parameters, Ph.D. thesis, Technische Universität Bergakademie Freiberg, 2015.

[42] C. D. Lorenz and R. M. Ziff, Precise determination of the bond percolation thresholds and finite-size scaling corrections for the sc, fcc, and bcc lattices, Phys. Rev. E **57**, 230 (1998).

[43] J. R. Taylor, *An Introduction to Error Analysis. The Study of Uncertainties in Physical Measurements*, 2nd ed. (University Science, Sausalito, CA, 1997).

[44] S. Iglauer, S. Favretto, G. Spinelli, G. Schena, and M. J. Blunt, X-ray tomography measurements of power-law cluster size

distributions for the nonwetting phase in sandstones, Phys. Rev. E **82**, 056315 (2010).

[45] Readers are directed to [13,39,40] for detailed comparisons of common approaches used to evaluate exponents from μCT data.

[46] T. Suekane, N. H. Thanh, T. Matsumoto, M. Matsuda, M. Kiyota, and A. Ousaka, Direct measurement of trapped gas bubbles by capillarity on the pore scale, Energy Procedia **1**, 3189 (2009).

[47] I. Chatzis and N. Morrow, Correlation of Capillary number relationships for sandstone, Soc. Petrol. Eng. J. **24**, 555 (1984).

[48] J. M. Ziman, The localization of electrons in ordered and disordered systems I. Percolation of classical particles, J. Phys. C **1**, 1532 (1968).

[49] R. Lenormand and C. Zarcone, Role of roughness and edges during imbibition in square capillaries, in *SPE Annual Technical Conference and Exhibition, Houston, Texas* (Society of Petroleum Engineers, 1984).

[50] G. N. Constantinides and A. C. Payatakes, Effects of precursor wetting films in immiscible displacement through porous media, Transport Porous Med. **38**, 291 (2000).

[51] J. Schmatz, J. L. Urai, S. Berg, and H. Ott, Nanoscale imaging of pore-scale fluid-fluid-solid contacts in sandstone, Geophys. Res. Lett. **42**, 2189 (2015).

[52] N. R. Morrow, The effects of surface roughness on contact angle with special reference to petroleum recovery, J. Can. Petrol. Technol. **14**, 42 (1975).

[53] H. H. Yuan, The influence of pore coordination on petrophysical parameters, in *SPE Annual Technical Conference and Exhibition, San Antonio, Texas* (Society of Petroleum Engineers, 1981).

[54] P. H. Valvatne and M. J. Blunt, Predictive pore-scale modeling of two-phase flow in mixed wet media, Water Resour. Res. **40**, W07406 (2004).